Environ Geol
DOI 10.1007/s00254-006-0601-x

ORIGINAL ARTICLE

Spatio-temporal estimation of shallow landslide hazard triggered by rainfall using a three-dimensional model

Cheng Qiu · Tetsuro Esaki · Mowen Xie · Yasuhiro Mitani · Chunxiang Wang

Received: 28 February 2006 / Accepted: 26 November 2006

Abstract A shallow landslide triggered by rainfall can be forecast in real-time by modeling the relationship between rainfall infiltration and decrease of slope stability. This paper describes a promising approach that combines an improved three-dimensional slope stability model with an approximate method based on the Green and Ampt model, to estimate the time–space distribution of shallow landslide hazards. Once a forecast of rainfall intensity and slope stability-related data, e.g., terrain and geology data, are acquired, this approach is shown to have the ability to estimate the variation of slope stability of a wide natural area during rainfall and to identify the location of potential failure surfaces. The effectiveness of the estimation procedures described has been tested by comparison with a one-dimensional method and by application to a landslide-prone area in Japan.

Keywords Landslide · Rainfall · Three-dimensional · Slope stability · Time–space distribution

Introduction

Shallow landslides are frequently observed in mountainous countries after intensive rainfall, resulting in the loss of life and costly damage to the environment. Any landslide hazard estimation system that is commonly used for hazard mitigation should give answers to three key questions: (1) the magnitude, (2) the location and (3) the time of occurrence.

The factors that determine a landslide can be summarized as falling into two categories: quasi-static variables and dynamic variables (Dai and Lee 2001). The quasi-static variables, such as geology, slope gradient, slope aspect, elevation, and geotechnical properties, contribute to landslide susceptibility and determine the location and the magnitude of the failure. The dynamic variables, such as rainfall and earthquake, tend to trigger landslides in an area of given susceptibility and thus have a direct impact on the time of occurrence of the landslide. It is necessary to evaluate the effects of both the quasi-static variables and the dynamic variables on slope stability (Wu and Sidle 1995; Crosta 1998).

The influence of rainfall on landslide has been a subject of research for many years (Liritano et al. 1998; Gasmo et al. 2000; Tsukamoto et al. 2002; Al-Homoud et al. 1999; Wilkinson et al. 2002; Kim et al. 2004). When a wide natural area is an object of study, much research has traditionally been focused on the relationship between the probability of landslide occurrence and the rainfall threshold (Finlay et al. 1997; Pedrozzi 2004), in which the rainfall threshold, defined as the rainfall required to cause one landslide in an area observed during past rainfall events, was used to predict the occurrence of slope failure. An intrinsic hypothesis underlying such methods is that the landslides analyzed exhibit consistent behavior. Therefore, a model established for a specific site is generally unreliable for application to a different site due to

C. Qiu (✉) · T. Esaki · Y. Mitani · C. Wang
Institute of Environmental Systems, Kyushu University, Hakozaki 6-10-1, Higashi Ku, Fukuoka 812-8581, Japan
e-mail: qiucheng@ies.kyushu-u.ac.jp

M. Xie
Civil and Environmental Engineering School, The University of Science and Technology Beijing, No. 30 Xueyuan Road, Haidian District, Beijing, China

variations in geotechnical conditions. Furthermore, such methods utilize rainfall as the only factor to provide warning and do not take other important variables influencing landslide, such as geology, geometry, and groundwater, into account.

Because shallow landslides always occur as the result of the infiltration of water from intense rainfalls, it is reasonable to evaluate this type of slope failure using physically based models to simulate the transient hydrological and geotechnical processes responsible for slope stability (Wu and Sidle 1995). However, most work has been limited to using a one-dimensional (1D) infinite slope equation to analyze slope stability for understanding local, on-site conditions (Collins et al. 1998; Cho and Lee 2002; Frattini et al. 2004). It is well known that a three-dimensional (3D) situation may become important in cases where the geometry of the slope and slip surface varies significantly in the lateral direction, the material properties are highly anisotropic, or the slope is locally loaded. Even though some 3D models of slope stability analysis have been proposed, a suitable method for application of 3D models to a wide area is still lacking. The reasons for the limited applicability of 3D models can be summarized as the difficulties in (1) creating continuously distributed data for topography, strata and groundwater through limited investigations; (2) processing a vast amount of complex information about the natural topography and geology; and (3) determining the location and the shape of an unknown failure surface.

A geographical information system (GIS) is a relatively new software tool for geotechnical engineers (Carraea et al. 1995). The capabilities of GIS range from conventional data storage to complex spatial analysis and graphical presentation. Commonly, GIS uses raster data for the storage, processing, display and analysis of spatial data. In raster data, each area is divided into rows and columns, which form a regular grid structure. Coincidentally, most 3D methods use a column-based method in which the failure mass is divided into a number of square columns. Combining the GIS raster data with the well-known column-based 3D model advised by Hovland (1977), an improved GIS raster-based 3D deterministic model has been proposed (Xie et al. 2006), in which all related data for slope stability analysis are transformed into GIS raster data and therefore can be easily stored, retrieved, displayed, and analyzed to calculate a safety factor. Even though this model would tend to lightly underestimate the normal force, and hence the shear resistance, on steep slip surfaces for frictional slopes, due to the neglect of the side forces on the vertical faces of the columns (Xie et al. 2006), the convenience of the computation for safety factor makes it suitable for evaluating the slope stability of a wide mountainous area.

This paper describes the development of the proposed model into a new GIS-based 3D model by incorporating an infiltration model and taking account of geomechanical changes of soil strength during rainfall in the calculation. Using this model, the location and the shape of critical slip surfaces can be identified through a random search procedure by varying the geometrical parameters of the ellipsoid that is used to simulate the shape of the slip surface. Furthermore, the time of occurrence of failures can be forecast by mapping the changing distribution of safety factors during rainfall.

Hydrological model

Infiltration is a function of soil properties, rainfall and local settings. Hydraulic characteristics and suction are the dominant soil properties, and rainfall intensity and duration are important characteristics leading to soil saturation. Other factors influencing the duration and quantity of the critical precipitation are soil moisture content and antecedent rainfall. There are numerous models formulated on the basis of soil characteristics that have been proposed to evaluate infiltration (Green and Ampt 1911; Neuman 1976; Smith et al. 1993; Ogden and Saghafian 1997; Iverson 2000). However, it is still difficult to quantify the amount of infiltration and the corresponding effect on the stability of slope for a regional area due to the complex mechanism and many parameters that are used in the models. Those available often require detailed geotechnical information on the existing conditions and long-time computation. Because of the high cost involved they are generally only achievable at the site investigation level in cases where high risk is anticipated. Therefore, a flexible model that is feasible for regional scale management and quick application, with suitable simplifications, is required.

Before the infiltrating rainfall meets the groundwater table or the impermeable zone, infiltration through an unsaturated zone can be approximately considered to be vertical. Therefore, the Green and Ampt model, as a 1D infiltration model that is based on widely accepted concepts of soil physics and is relatively easy to use, is adopted in this study.

The Green and Ampt method, which was published 95 years ago (Green and Ampt 1911), remains popular to this day because of its succinct concept of the ''piston'' wetting front and the inclusion of soil suction head and hydraulic conductivity parameters. Four

assumptions are made in this model: (1) soil surface is maintained constantly wet by water ponding; (2) a sharp wetted front exists; (3) the hydraulic conductivity is constant through the soil; and (4) the soil matrix suction at the front remains constant. These assumptions mean that the soil is fully saturated from the surface to the depth of the wetting front, while the soil below the wetting front is at the initial degree of saturation.

As shown in Fig. 1, according to Darcy's law, the infiltration rate is given by:

$$f = K_s \frac{\psi_f + Z_f}{Z_f} \tag{1}$$

The depth of the wetting front can be related to the cumulative amount of infiltrated water by

$$F = Z_f(\theta_s - \theta_i) \tag{2}$$

Rearranging Eq. 2 to solve for Z_f and applying it to Eq. 1, the infiltration rate at any time t becomes:

$$f(t) = K_s + K_s \frac{\psi_f(\theta_s - \theta_i)}{F} \tag{3}$$

The expression of $F(t)$can be stated as follows:

$$t = t_p + \frac{1}{K_s}\left[F - F_p + \psi_f(\theta_s - \theta_i)\ln(n)\right] \tag{4}$$

$$n = \frac{\psi_f(\theta_s - \theta_i) + F_p}{\psi_f(\theta_s - \theta_i) + F} \tag{5}$$

t_p andF_p can be calculated from the following equations:

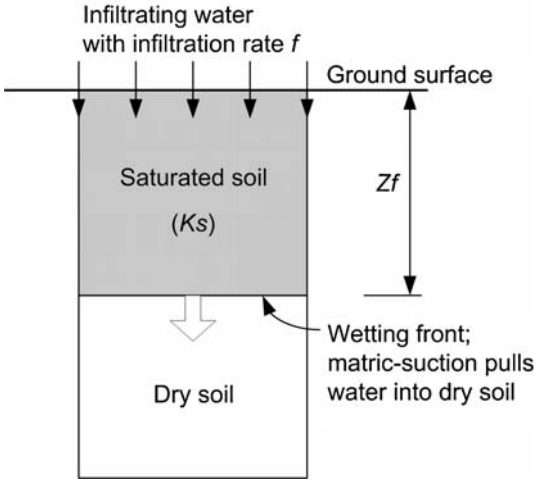

Fig. 1 Conceptual view of the Green and Ampt infiltration model

$$t_p = \frac{F_p}{P} \tag{6}$$

$$F_p = \frac{\psi_f K_s(\theta_s - \theta_i)}{P - K_s} \tag{7}$$

where $f(t)$ is the infiltration rate (m/h) at time t (h), K_s the soil aturated hydraulic conductivity (m/h), ψ_f the matrix suction at the wetting front (m), Z_f the depth of the wetting front (m), F the cumulative amount of infiltrated water (m), θ_s the soil saturated volumetric water content, θ_i the initial soil volumetric water content, t_p the time when water begins to pond on the soil surface (h), F_p the amount of water that infiltrates before water begins to pond at the surface (m), and P the rainfall rate (m/h).

It should be noted that a necessary condition for Eqs. 3–7 is that the rainfall rate must be greater than the soil hydraulic conductivity. If the rainfall rate is not greater than the potential infiltration rate ($P \le K_s$) or no surface ponding occurs ($t \le t_p$), then all rainfall will infiltrate into the soil without runoff, and the actual infiltration rate is equal to the rainfall rate:

$$f(t) = P \tag{8}$$

$$F = Pt \tag{9}$$

Parameters of a typical soil used in the equations above can be obtained from a geotechnical test or from the literature (Ranwls et al. 1983; Ogden and Saghafian 1997).

Unfortunately, an iterative procedure is needed to calculate the infiltrated depth at a specific time because Eq. 4 is not expressed explicitly as a function of time and the cumulative infiltration. Serrano (2003) proposed an approximate formula that can yield a solution very close to the exact solution under the condition that the rainfall rate is not very high relative to the soil saturated hydraulic conductivity:

$$F(t) \approx F_0(t) + \psi_f(\theta_s - \theta_i)\ln(m_1(t)) \times \left(1 + \frac{m_2(t)}{[1 - m_2(t)]\{1 + m_2(t)\ln[m_1(t)]\}}\right) \tag{10}$$

$$F_0 = K_s(t - t_p) + F_p \tag{11}$$

$$m_1(t) = \frac{F_0(t) + \psi_f(\theta_s - \theta_i)}{F_p + \psi_f(\theta_s - \theta_i)} \tag{12}$$

$$m_2(t) = \frac{\psi_f(\theta_s - \theta_i)}{F_0(t) + \psi_f(\theta_s - \theta_i)} \tag{13}$$

In general, excellent agreement can be obtained between solutions of Eqs. 10 and 4 when the following equation is satisfied:

$$2m_2(t) < 1 \tag{14}$$

Figure 2 illustrates a comparison between the exact solution of Eq. 4 and the approximate solution of Eq. 10, which was also done by Serrano (2003). The following parameter values were used: $P = 2$ (cm/h); $K_s = 1$ (cm/h); $\psi_f = 10$ (cm); $\theta_i = 0.1$; $\theta_s = 0.4$.

The flowchart of the infiltrated depth calculation for the duration T of rainfall is illustrated by Fig. 3. $F^*(i)$ can be calculated by Eq. 10 or by Eq. 4, depending on whether the condition of Eq. 14 is satisfied or not, respectively.

The GIS-based 3D model

The mechanism underlying the proposed GIS-based 3D model is illustrated in Fig. 4. A potentially sliding mass, which will be the study object, is shown in Fig.4a. Initially, all the discrete investigation data for the study site can be represented as a number of GIS vector layers (e.g., a line layer of contour), and then converted to GIS raster layers through spatial interpolation, as shown in Fig. 4b. GIS raster data are composed of one or more equally spaced cells, whose values usually record one property of a geographic phenomenon occurring over the patch of space it covers. Each raster layer represents a certain type of information such as topography, stratum, or groundwater. Furthermore, the superposed construction of the strata can be presented by overlay of the multiple raster layers. The overlay extends the 2D raster layers to a third dimension, which makes the application of 3D engineering models possible. Each cell is a local position and can be

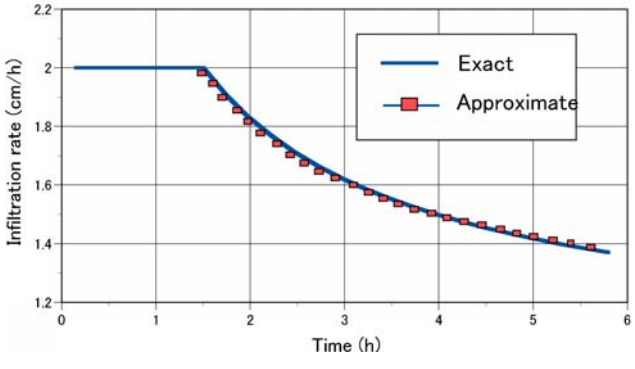

Fig. 2 Comparison between approximate and exact solutions for infiltration rate

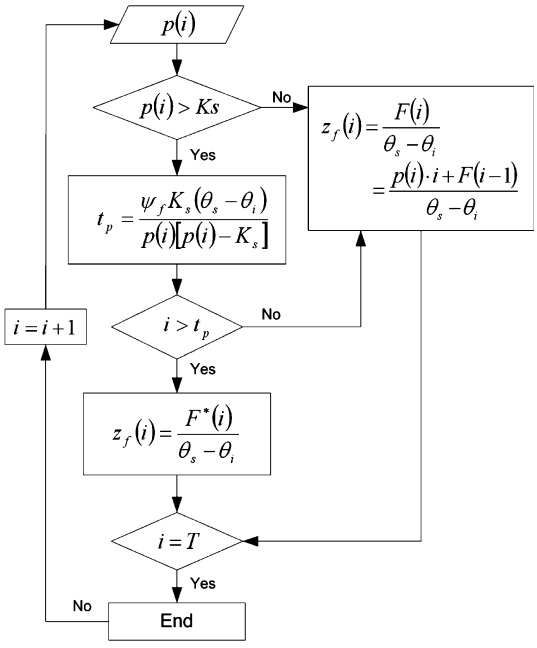

Fig. 3 Flowchart of infiltrated depth calculation during duration T of rainfall

imaged to a 3D column that consists of several layers. The elevations of the ground surface and all the soil surfaces at the same x and y coordinates define the positions of the ground surface and the soil surfaces within the 3D column.

Here, the GIS raster model is manipulated to accommodate the traditional column-based 3D model by discretization of the study mass, as shown in Fig. 4c. Slope stability analysis-related information for each soil column, such as topography, strata, groundwater, faults, can thus be obtained from the corresponding cell of raster layers (Fig. 4d) and used to calculate a safety factor.

Integrating Hovland's (1977) 3D model and the GIS raster-based database, the safety factor can be derived from the horizontal force equilibrium in the direction of sliding (Xie et al. 2003):

$$\mathrm{SF}_{3\mathrm{D}} = \frac{\sum_J \sum_I (cA + W\cos\theta\tan\phi)\cos\theta_{\mathrm{Avr}}}{\sum_J \sum_I W\sin\theta_{\mathrm{Avr}}\cos\theta_{\mathrm{Avr}}} \tag{15}$$

where $\mathrm{SF}_{3\mathrm{D}}$ is the 3D safety factor of the slope,, c the cohesion (kN/m^2), A the area of the slip surface (m^2), W the weight of one soil column (kN), φ the friction angle (°), θ the inclination of the slip surface (°), θ_{Avr} the angle between the direction of movement and the horizontal plane (°); and J,I are the numbers of rows and columns of the cell within the range of failure mass.

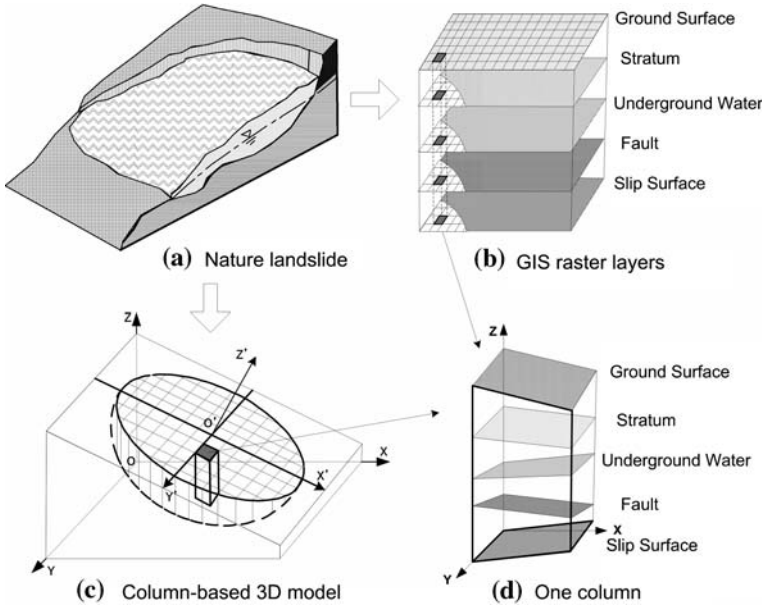

Fig. 4 The mechanism of GIS raster-based 3D model

It should be noted that the direction of the horizontal force equilibrium in Eq. 15 can be the real direction of sliding, but not be parallel with the *y*-coordinate direction that was used in the original Hovland's (1977) model. This allows the model to deal with a wide area where various sliding directions can appear.

To identify critical slip surfaces from the study area, a random search is performed by means of a minimization of the 3D safety factor. The shape of the slip surface is assumed to be the lower part of an ellipsoid and will vary in depth, dip angle, and direction of inclination. If a randomly produced slip surface, based on the lower part of an ellipsoid, is lower than a weak discontinuous surface or the confines of the hard stratum, the weak discontinuity or the confined surface of the hard stratum will be prioritized for selection as one part of the assumed slip surface. The direction of inclination is calculated as the mode value from the dip direction (Aspect in GIS) of all raster cells in the range of the sliding mass. The uncertain parameters, such as dip angle and the *a*, *b*, and c axes, are specified by Monte Carlo simulation from the range they may take (Xie et al. 2004). For each cell that is taken as the central point of a randomly chosen trial ellipsoid from the range of sliding mass, a minimum safety factor and a critical slip surface can be obtained after enough time of calculations.

It is widely known that rainfall causes a rise of groundwater level as well as an increase in pore water pressure that results in slope failure. However, in many situations where shallow failures are concerned, it has been noted that the failure was attributed to the advance of a wetting front into the slope instead of a rise of the groundwater level (Ng et al. 2001; Cho and Lee 2002; Kim et al. 2004). The wetting front causes a reduction in soil suction (or negative pore pressure) and an increase in the weight of soil per unit volume. These result in a process in which soil resistant strength decreases while total stress increases, until failure occurs on the potential failure surface where equilibrium cannot be sustained.

Under these conditions, there are four possible situations regarding the slip surface that can be anticipated, and four models are thus proposed to calculate the corresponding safety factors.

Model 1: The slip surface forms in the unsaturated zone between the wetting front that is advancing from the ground surface and the groundwater table, as shown in Fig. 5. In this situation, the horizontal resistance force F_1 and the horizontal sliding force F_2 acting on the slip surface can be calculated using Eqs. 16 and 17, respectively:

$$F_1 = \left\{c_i' A' + [\gamma_i z + (\gamma_{\text{sat}} - \gamma_i) H_w] A \cos\theta \tan\phi'\right\} \cos\theta_{\text{Avr}} \tag{16}$$

$$F_2 = [\gamma_i z + (\gamma_{\text{sat}} - \gamma_i) H_w] A \sin\theta_{\text{Avr}} \cos\theta_{\text{Avr}} \tag{17}$$

Model 2: The slip surface forms in the saturated zone between the ground surface and the wetting front that is advancing from the ground surface, as shown in Fig. 6. In this situation, the horizontal resistance force F_1 and the horizontal sliding force F_2 can be calculated using Eqs. 18) and 19, respectively:

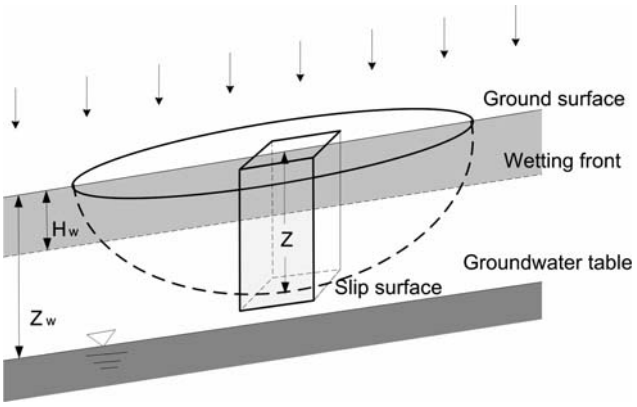

Fig. 5 Model1: slip surface forms between the wetting front and the groundwater table

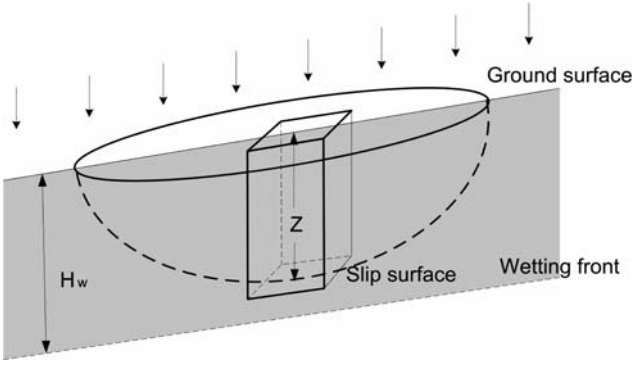

Fig. 6 Model2: slip surface forms between the ground surface and the wetting front

$$F_1 = \left[c'_w A' + (\gamma_{\text{sat}} z \cos\theta - u_w) A \tan\phi'\right] \cos\theta_{\text{Avr}} \quad (18)$$

$$F_2 = \gamma_{\text{sat}} z A \sin\theta_{\text{Avr}} \cos\theta_{\text{Avr}} \quad (19)$$

Model 3: The slip surface forms in the saturated zone under the groundwater table and the wetting front that has reached the groundwater table, as shown in Fig. 7. The horizontal resistance force F_1 and the horizontal sliding force F_2 can be calculated using Eqs. 18 and 19, respectively.

Model 4: The slip surface forms in the saturated zone under the groundwater table and the unsaturated zone exists between the wetting front and the groundwater table, as shown in Fig. 8. In this situation, the horizontal resistance force F_1 and the horizontal sliding force F_2 can be calculated using Eqs. 20 and 21, respectively:

$$F_1 = \left\{c'_w A' + \left[\left(\gamma_i (z_w - H_w) + \gamma_{\text{sat}} (H_w + z - z_w)\right) \times \cos\theta - u_w\right] A \tan\phi'\right\} \cos\theta_{\text{Avr}} \quad (20)$$

$$F_2 = \left[\gamma_i (z_w - H_w) + \gamma_{\text{sat}} (H_w + z - z_w)\right] A \sin\theta_{\text{Avr}} \cos\theta_{\text{Avr}} \quad (21)$$

Assuming that the vertical sides of each soil column are frictionless, the 3D safety factor can thus be calculated by summing F_1 and F_2 of all soil columns of failure mass:

$$\text{SF}_{\text{3D}} = \frac{\sum_J \sum_I F_1}{\sum_J \sum_I F_2} \quad (22)$$

where SF_{3D} is the 3D safety factor of the slope, F_1 the horizontal resistance force (kN), F_2 the horizontal sliding force (kN), γ_{sat} the saturated unit weight of soil (kN/m^3), γi the initial unit weight of soil (kN/m^3), c'_i the initial effective cohesion of soil (kN/m^2), c'_w the saturated effective cohesion of soil (kN/m^2), φ' the effective friction of soil (°), z_w the depth of the wetting front (m), H_w the depth of the groundwater table (m), z the depth of the slip surface (m), u_w the pore stress (kN/m^2), A the area of the soil column (m^2), A' the area of the slip surface of the soil column, θ the inclination of the slip surface (°), θ_{Avr} the dip angle of the main sliding direction (°), and J, I are the numbers of rows and columns of the cell in the range of failure mass.

It should be noted that in Eq. 22, F_1 and F_2 of each soil column would be calculated using the appropriate equation from Eqs. 16 to 21, depending on the different conditions described above.

The parameters necessary for the analysis can be obtained from triaxial and consolidation test data. If such data are not available, these parameters could be estimated from values and relationships determined by previous investigators.

Computational complementation

Figure 9 illustrates the computational procedures for estimation of rainfall-induced slope stability. For a given rainfall intensity, the permeation depth at a specified time can be predicted by the infiltration model described above. At the same time, taking a cell of the raster dataset to be the central point of an ellipsoid, a trial slip surface can be formed using the Monte Carlo simulation model. A safety factor is calculated subsequently by the 3D slope stability model, depending on the relationship between the permeation depth and the location of the slip surface. After many trials, the critical slip surface and the associated safety factor, which is the minimum of all the trial calculations, can

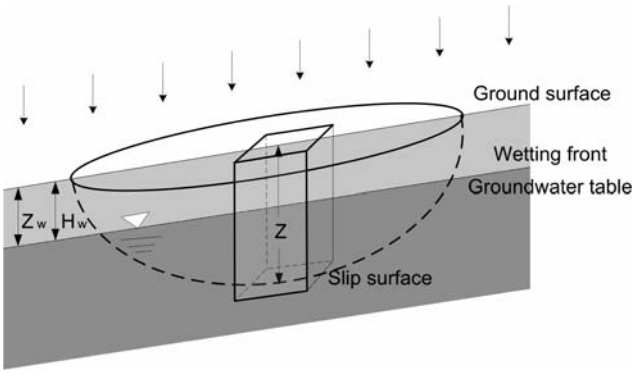

Fig. 7 Model3: slip surface forms under the groundwater table

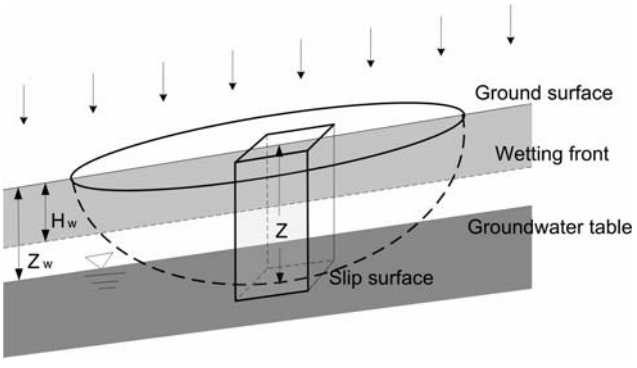

Fig. 8 Model4: slip surface forms under the groundwater table and the unsaturated zone exists

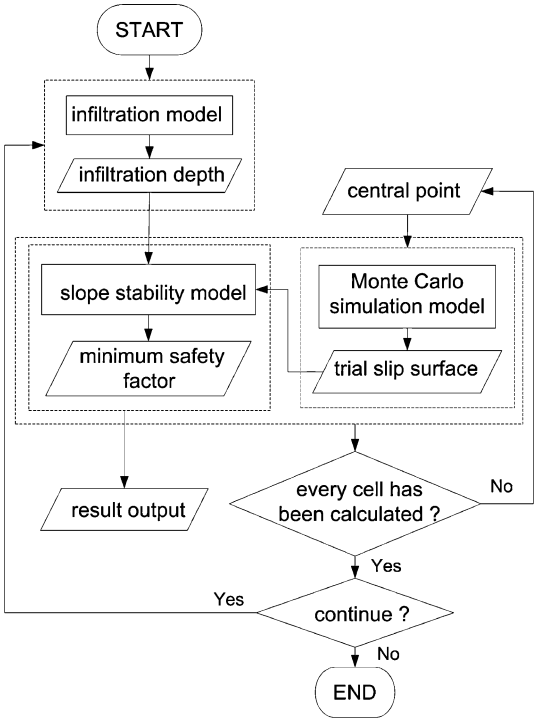

Fig. 9 Flow chart of rainfall-induced slope stability calculation

be obtained. The safety factor is then saved to a point dataset as the safety factor of the raster cell. Also, if the safety factor is <1, the information for the corresponding critical slip surface, such as location, shape, and volume, will be saved in the format of a polygon. In this way, the safety factor at a specified time can be calculated for all raster cells inside the slide mass range. As a result, the time of occurrence of a landslide can be predicted by means of the decrease of the safety factor along with the amount of rainfall, and the location and the magnitude of the potential slip surfaces can be known from the polygon dataset of critical slip surfaces.

All of the above calculations, including the infiltration model, the Monte Carlo simulation model and the slope stability model, have been incorporated within a GIS-based system, called the 3D slope stability analysis system (3DSSAS), which is programmed by Visual Basic language using Microsoft component object model (COM) technology. COM is a protocol that can be used to build reusable software components that are interchangeable in distributed systems at the binary level. In 3DSSAS, ArcObjects, the framework that forms the foundation of the ArcGIS^{TM} applications (GIS software developed by ESRI) with more than 2,000 COM-based components has been used.

Applications

A homogenous slope with a presumptive slip surface

The 3D method proposed here has been applied to a homogenous slope with a shallow weathering layer of residual soil overlying a bedrock interface. A presumptive 3D failure surface, which was extended directly from the 2D profile shown in Fig. 10, is generated from a sphere and a plane parallel with ground with a depth of 2 m, as shown in Fig. 11. The parameters used for infiltration calculation and slope stability analysis are: K_s= 1.87 cm/h; ψ_f =55 cm;$\nabla\theta = \theta_s - \theta_i = 0.28$; γ_i =14 kN/m^3;γ_{sat} = 16 kN/m^3; c'_i = 3 kN/m^2; c'_w = 2 kN/m^2; and φ' = 24°.

For uniform rainfall with different intensities of p = 4 cm/h and p = 8 cm/h, the 3D safety factor of assumed slip mass was calculated by the proposed model. The results are presented in Fig. 12, which shows a decrease in the safety factor from the time of rainfall began to the time that the wetting front reached the bedrock. It can be seen that the safety factor decreases rapidly for wetting front near the bedrock, and the rate of decrease of the safety factor is associated with rainfall intensity.

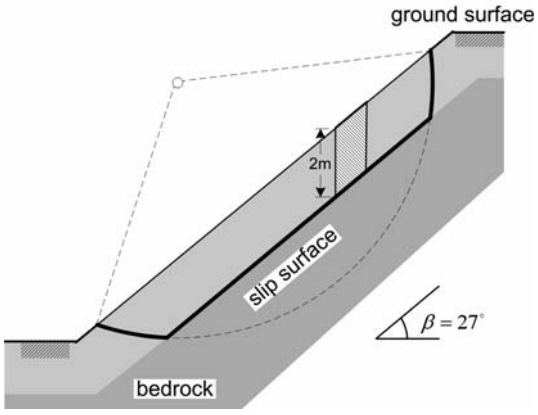

Fig. 10 Section view of a homogenous slope with presumptive failure surface

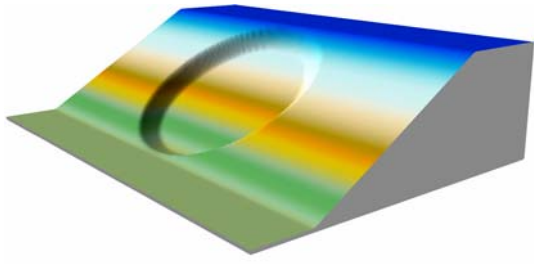

Fig. 11 3D view of the presumptive failure surface

In order to demonstrate the importance of the 3D shape effects of failure surface, a 1D analysis was performed for the presumptive failure surface to provide a direct comparison with the results of the 3D analysis. A modified 1D formula was used to calculate the 1D safety factor:

$$\mathrm{SF}_{1\mathrm{D}} = \frac{c' + [H_w\gamma_{\mathrm{sat}} + (z - H_w)\gamma_i]\cos^2\beta\tan\phi'}{[H_w\gamma_{\mathrm{sat}} + (z - H_w)\gamma_i]\sin\beta\cos\beta} \qquad (23)$$

where γ_{sat} is the saturated unit weight of soil (kN/m^3), γ_i the initial unit weight of soil (kN/m^3), c' the effective cohesion of soil (kN/m^2), φ' the effective friction of soil (°), H_w the depth of the wetting front (m), z the depth of the slip surface (m), and β the inclination of the slip surface (°). Figure 13 illustrates a relationship between the depth of the wetting front and the safety factors obtained by the 1D and the 3D analysis. It can be seen that both 1D safety factors and 3D safety factors decrease with development of the wetting front. It should be noted that the safety factors obtained from the 3D method proposed here without considering the shearing resistance along the vertical slides of the slide mass, are similar to the safety factors from the 1D analysis at the initial state. But, as the depth of the wetting front

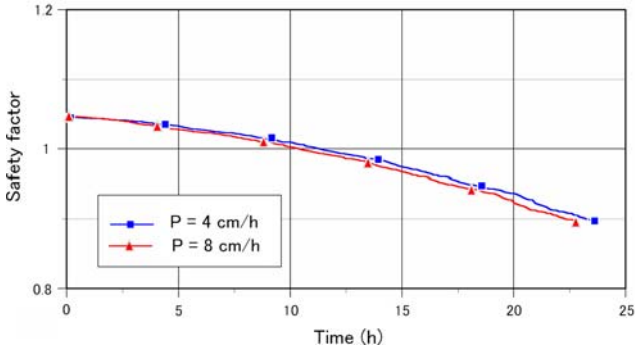

Fig. 12 Influence of rainfall intensity on 3D safety factor

increases, the decrease of the curve for the 3D safety factor is remarkably rapid compared to that for the 1D safety factor. This suggests that the effect of rainfall infiltration can result in a significant difference between the 1D and 3D safety factors, even for a simple, sheet-shaped failure surface. A 1D analysis yields a conservative estimate of the safety factor, because the shear resistance along the two sides of the slide mass and/or end effects cannot be included in the calculation.

A practical application

The Goto section of National Route 49 is located near the city of Iwaki in Japan, about 10 km westward, where slope disasters have happened frequently. To forecast slope failure and to provide support for deciding on suitable countermeasures, the system described here was used for landslide mapping.

The bedrock of the study area is represented by Mesozoic granites, which is hard in a fresh state but often heavily weathered to form deep residual deposits. The soil cover in the area, with an average depth of about 2 m, is composed mainly of colluvium and residual deposits formed by weathering of granites and

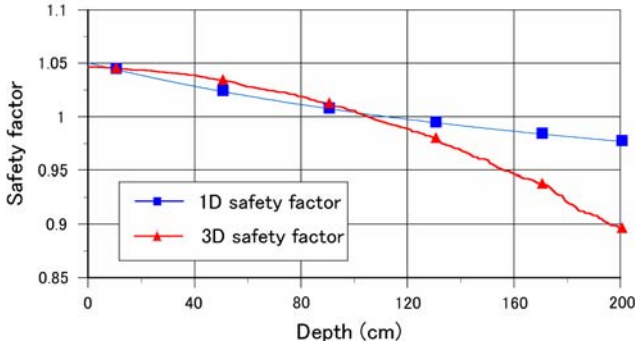

Fig. 13 Variation of 1D and 3D safety factors with depth of wetting front

Table 1 Geomechanical and hydraulic parameters of the surficial soil

c_i' (kN/m^2)	c_W' (kN/m^2)	φ' (°)	γ_i (kN/m^3)	γ_w (kN/m^3)	K_s (cm/h)	ψ_f (cm)	$\nabla\theta$
14.5	3.2	40.4	15.3	16.5	5.2	40.8	0.31

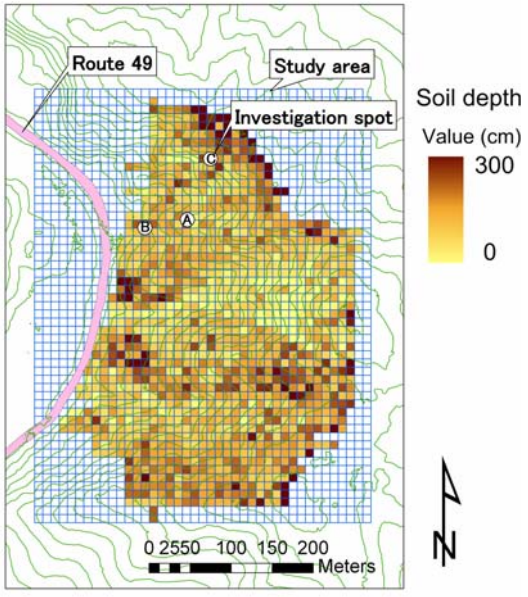

Fig. 14 Distribution of surficial soil depth and location of investigation spots

accumulation of debris as result of landslide activity. It is well known that landslides are common in colluvium and residual soils, particularly during periods of intense rainfall. The well-developed internal drainage of the soils is conducive to water infiltration, subsequent reduction in pore-water tension, and consequent sliding. According to the characteristics of the geological formation, the possible collapse mode was considered

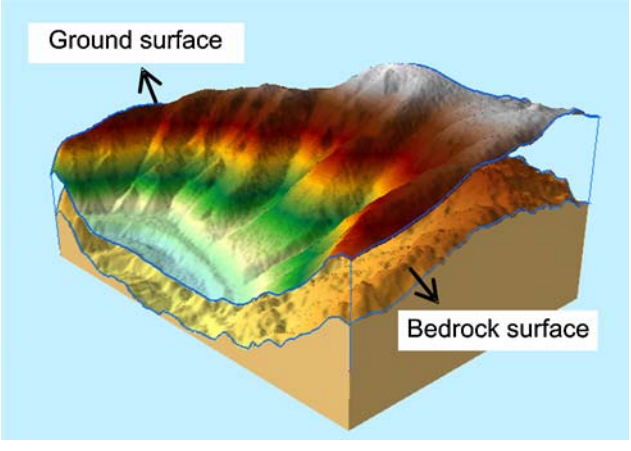

Fig. 15 3D view of bedrock surface with ground surface covering

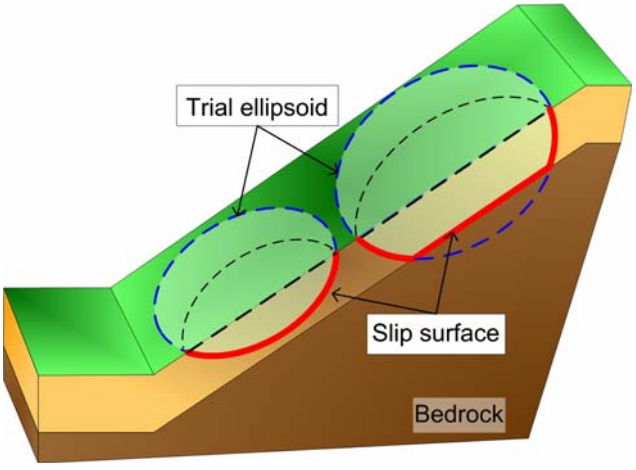

Fig. 16 Two types of possible slip surface

to be a shallow slope failure with a sliding surface along the boundary surface of the bedrock or inside the soil layer.

The surface digital elevation model (DEM) data in grid form with 2 m mesh size was produced from airborne laser scanning. The geomechanical and hydraulic parameters of the soil surface consisted of information from a specific geotechnical field investigation, triaxial test results of soil samples collected from three spots, and related literature, as shown in Table 1. In addition, detailed data for soil depth, with a precision of one value per 10 m^2, were obtained by a special surveying method using a probe stick. The distribution of the soil depth and the location of the sites where the soil samples were collected are shown in Fig. 14. The bedrock surface was then abstracted as a GIS raster dataset by subtraction of the surface elevation and the soil depth. Figure 15 shows a 3D view of the topography of the bedrock surface with ground surface covering.

For the study area, a uniform rainfall event with a duration of 10 h and an intensity of 8 cm/h was assumed, and the method proposed above was applied. The detection of the critical slip surface was achieved through trial searching and calculation of the 3D safety factor. In the trial searching process, if the lower part of a randomly produced ellipsoid is lower than the boundary surface of the bedrock, the confined surface of the bedrock will be prioritized for selection as one part of the assumed slip surface. Figure 16 illustrates two types of assumed slip surface either formed by the

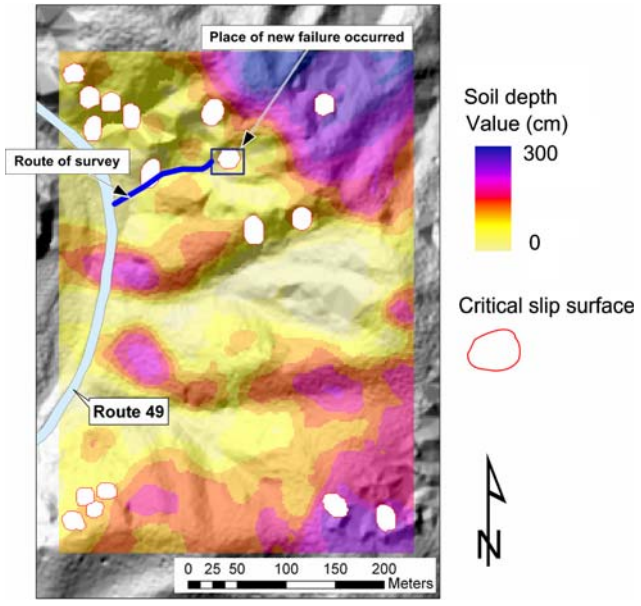

Fig. 17 Distribution of surficial soil depth with identified slip surfaces

lower portion of an ellipsoid or composed partially of an ellipsoid and the boundary interface of the bedrock. After 100 trial calculations for each raster cell taken as the central point of a trial ellipsoid in the study range, finally, the critical slip surfaces were identified, and the variation of safety factors over time was mapped. The distribution of the critical slip surfaces that have a safety factor <1 and the depth distribution of the residual soil are shown in Fig. 17. The critical slip surfaces are seen frequently in parts where the depth of soil is about 1.5 m, and the slope angle is around 35°–50°. In a field investigation, it was discovered that a new slope failure occurred at very close location to an identified slip surface which is marked in Fig. 17. It demonstrated the accuracy of the calculating result on some level, even though the causation of the failure can not be said to be rainfall due to unknown of the time of failure occurrence. Figure 18 illustrates six distribution maps of the safety factors changing over time. From these maps, a high correlation between rainfall and the decrease of the safety factor can be recognized.

Conclusions

By combining an infiltration model with an improved column-based 3D slope stability analysis model, a new GIS-based 3D model has been developed for evaluating the variation of surficial slope stability during a rainfall event. A comparison between the results of the

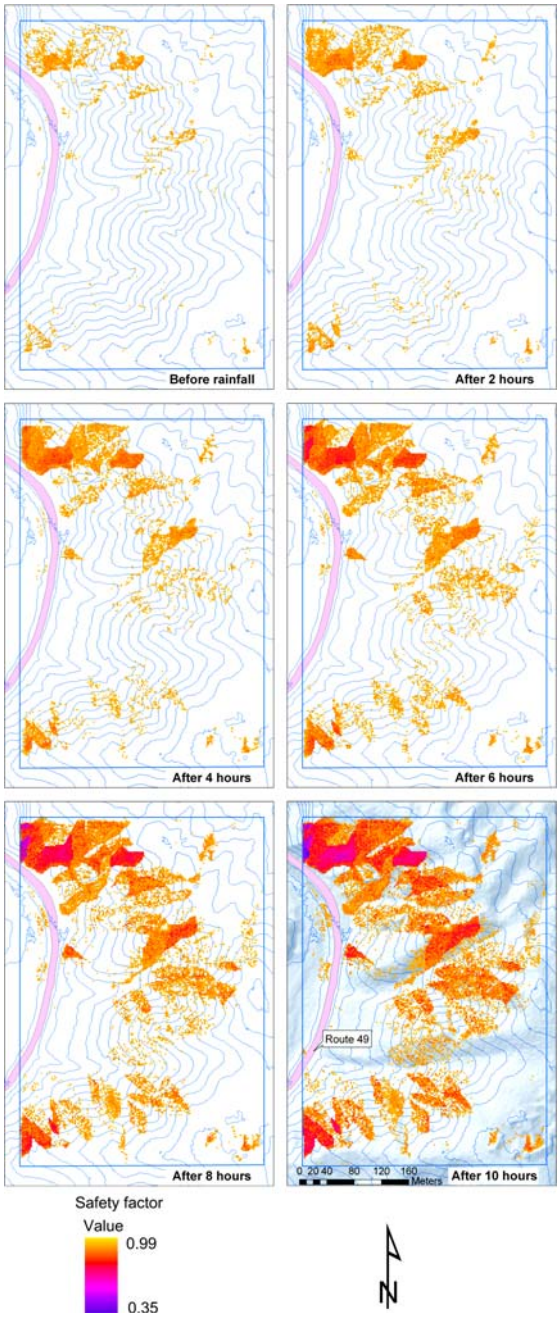

Fig. 18 Distribution maps of safety factors changing over time

proposed model and those obtained by a 1D model indicated that 3D methods are more sensitive to the failure introduced by rainfall infiltration. The reason for the larger reduction of the safety factor in the 3D case is a consequence of the fact that 3D slip surfaces include a large proportion of the marginal part where the reduction of the resistant force happens before infiltrated water reaches the bottom of the slip surface.

The 3DSSAS program has been developed to carry out all the processes, including data handling, calcula-

tion, and expression of the results. The introduction of the GIS technology enables both a convenient management of enormous amounts of slope-related data and an easy implementation of complicated calculations.

The suitability of the proposed method for large complex and data-limited natural terrains was demonstrated by a practical case study, in which the distribution of the safety factors changing over time and the location of the critical slip surfaces were mapped. Such a spatio-temporal hazard map of rainfall-induced landslide has profound implications for the identification of the resultant processes that control slope stability and specification of remedial and stabilization measures.

It should be noted that the present study was focused on investigating the effect of infiltration of a uniform rainfall. Other effects, such as antecedent precipitation and run-off, which can influence the rate and the amount of infiltration significantly, should be considered in a future study.

References

Al-Homoud AS, Prior G, Awad A (1999) Modeling the effect of rainfall on instabilities of slopes along highways. Environ Geol 37(4):317–325

Carraea A, Cardinsli F, Guzzetti M, Reichenbach P (1995) GIS technology in mapping landslide hazard, geographical information systems in assessing natural hazards [M]. Kluwer, Dordrecht, Netherlands, pp 135–175

Cho SE, Lee SR (2002) Evaluation of surficial stability for homogeneous slopes considering rainfall characteristics. J Geotech Geoenviron Eng 128(9):756–763

Collins BD, Znidarcic D (1998) Slope stability issues of rainfall induced landslides. In: Maric B, Lisac Z, Szavits-Nossan A (eds) Geotechnical hazards, XI Danube-European conference on soil mechanics and geotechnical engineering, Porec, Croatia, Balkema, Rotterdam, pp 791–798

Crosta G (1998) Regionalization of rainfall thresholds: an aid to landslide hazard evaluation. Environ Geol 35(2–3):131–145

Dai F, Lee C (2001) Terrain-based mapping of landslide susceptibility using a geographical information system: a case study. Can Geotech J 38:911–923

Finlay PJ, Fell R, and Maguire PK (1997) The relationship between the probability of landslide occurrence and rainfall. Can Geotech J 34:811–824

Frattini P, Crosta GB, Fusi N, Negro P (2004) Shallow landslides in pyroclastic soils: a distributed modeling approach for hazard assessment. Eng Geol 73:277–295

Gasmo JM, Rahardjo H, Leong EC (2000) Infiltration effects on stability of a residual soil slope. Comput Geotech 26:145–165

Green WH, Ampt GA (1911) Studies of soil physics: I. The flow of air and water through soils. J Agric Sci 4:1–24

Hovland HJ (1977) Three-dimensional slope stability analysis method. J Geotech Eng, Division Proceedings of the American Society of Civil Engineers[C]. Pacific Gas and Electric Co., San Francisco, California, 103(GT9):971–986

Iverson RM (2000) Landslide triggering by rain infiltration. Water Resour Res 36(7):1897–1910

Kim J, Jeong S, Park S, Sharma J (2004) Influence of rainfall-induced wetting on the stability of slopes in weathered soils. Eng Geol 75:251–262

Liritano G, Versace P, Sirangelo B (1998) Real-time estimation of hazard for landslides triggered by rainfall. Environ Geol 35(2–3):175–183

Neuman SP (1976) Wetting front pressure head in the infiltration model of Green and Ampt. Water Resour Res 12(3):564–566

Ng CWW, Wang B, Tung YK (2001) Three-dimensional numerical investigations of groundwater responses in an unsaturated slope subjected to various rainfall patterns. Can Geotech J 38:1049–1062

Ogden F, Saghafian B (1997) Green and Ampt infiltration with redistribution. J Irrig Drain Eng 123(5):386–393

Pedrozzi G (2004) Triggering of landslides in Canton Ticino (Switzerland) and prediction by the rainfall intensity and duration method. Bull Eng Geol Environ 63:281–291

Rawls WJ, Brakensiek DL, Miller N (1983) Green–Ampt infiltration parameters from soils data. J Hydraul Eng 109(1):62–70

Serrano SE (2003) Improved decomposition solution to Green and Ampt equation. J Hydrol Eng 8(3):158–160

Smith RE, Corradini C, Melone F (1993) Modeling infiltration for multistorm runoff events. Water Resour Res 29:133–144

Tsukamoto Y, Ishihara K, Nosaka Y (2002) On the initiation of rainfall induced soil failure. In: Maric, Lisac, Szavits-Nossan (eds) Geotechnical hazards. Balkema, Rotterdam, pp 883–890

Wilkinson P, Anderson M, and Lloyd D (2002) An integrated hydrological model for rain-induced landslide prediction. Earth Surf Process Landforms 27:1285–1297

Wu W, Sidle RC (1995) A distributed slope stability model for steep forested basins. Water Resour Res 31(8):2097–2110

Xie M, Esaki T, Cai M (2004) A GIS-based method for locating the critical 3D slip surface in a slope. Comput Geotech 31:267–277

Xie M, Esaki T, Qiu C, Wang C (2006) Geographical information system-based computational implementation and application of spatial three-dimensional slope stability analysis. Comput Geotech 33:260–274